ENERGY DEPOSITION AND MELT DEFORMATION ON THE ITER FIRST WALL DUE TO DISRUPTIONS AND VERTICAL DISPLACEMENT EVENTS

J. COBURN, M. LEHNEN, R.A. PITTS, G. SIMIC, F.J. ARTOLA
ITER Organization
St. Paul-lez-Durance, France
Email: richard.pitts@iter.org

E. THORÉN, S. RATYNSKAIA
Space & Plasma Physics - KTH Royal Institute of Technology
Stockholm, Sweden

K. IBANO
Graduate School of Engineering, Osaka University
Osaka, Japan

M. BRANK, L. KOS
LECAD Laboratory, Univ. of Ljubljana
Ljubljana, Slovenia

R. KHAYRUTDINOV, V.E. LUKASH
National Research Centre "Kurchatov Institute"
Moscow, Russia

B. STEIN-LUBRANO
Plasma Science and Fusion Center, MIT
Massachusetts, USA

E. MATVEEVA
Institute of Plasma Physics of CAS
Prague, Czechia

G. PAUTASSO
Max Planck Institute for Plasma Physics Garching
Garching, Germany

Abstract

An analysis workflow has been developed to assess energy deposition and material damage for ITER vertical displacement events (VDE) and major disruptions (MD). The VDEs and MDs are modeled in DINA with variations in plasma current I_p, disruption direction (upwards or downwards), Be impurity density n_{Be}, and diffusion coefficient χ. SMITER field-line tracing calculates time-dependent, 3D maps of surface power density $q_\perp$ on the Be-armored first wall panels (FWP) for the current quench phase of each disruption. MEMOS-U determines the temperature response, predicting the extent, depth, and $\vec{J}x\vec{B}$ motion of molten Be on each FWP surface. Effects of Be vapor shielding are included. The 15MA/5.3T scenarios show the most extreme melt damage, with the assumed n_{Be} exhibiting a strong effect on the disruption duration, peak $q_\perp$ and total energy deposition to the first wall. The worst-cases are upward 15MA VDEs and MDs at lower values of n_{Be}, with $q_{\perp,max} = 307\ MW/m^2$ and maximum erosion thickness losses of ~2mm after timespans of about 400-500ms. All 5MA scenarios avoided melt damage, and only one 7.5MA scenario gives a notable erosion depth of 0.25mm. These results imply that disruptions during 5MA, and some 7.5MA, operating scenarios will be acceptable during the Pre-Fusion Power Operation phases of ITER.

1. INTRODUCTION

Unmitigated thermal and electromagnetic loads from major plasma disruptions (MDs) and vertical displacement events (VDEs) pose a serious risk to ITER plasma-facing components (PFC). Potential damage from disruptions is one of the key drivers for the development of an effective Disruption Mitigation System (DMS). Together with ELM control systems, a well-practiced Plasma Control System (PCS), and proper disruption avoidance strategies, the DMS will ensure the integrity of the beryllium (Be) and tungsten-armored PFCs over the course of ITER operations. ITER will operate with a Staged Approach [1]. After completion of the First Plasma phase, the beryllium first-wall panels (FWPs) and tungsten (W) divertor cassettes will be installed in the vacuum vessel for the first Pre-Fusion Power Operations phase (PFPO-1). PFPO-1 will establish diverted plasma operations with H or He plasmas, up to at least 7.5 MA / 2.65 T in L-mode, with the possibility of 5MA/1.8T H-mode. The second

Pre-Fusion Power Operations phase, PFPO-2, will focus on system commissioning to reach full-power, 15MA/5.3T L-mode and H-mode operations with H or He plasmas. Finally, the Fusion Power Operations (FPO) phase will demonstrate full-power H-mode operations with a D-T plasma and produce net fusion energy gain, in the range of Q = 5 – 10. The FWPs and divertor cassettes installed before the start of PFPO-1 will remain in ITER through FPO.

The question arises: how early in the Staged Approach will PFC damage from unmitigated disruptions and VDEs become problematic? Intentional VDEs will actually be required during PFPO phases to calibrate EM load diagnostics, and the learning process for the DMS will inevitably lead to unexpected impacts on the first wall (FW). Thus, some of the PFC lifetime may be consumed before FPO even commences. Although the achievable thermal energies in PFPO-1 and -2 will be low compared to FPO, the stored magnetic energy will reach its maximum when approaching 15MA/5.3T operations. The heat loads on PFCs arising from the loss of magnetic energy during the current quench phase of unmitigated MDs and VDEs can be substantial and are the topic of this paper.

A workflow has been developed to assess energy deposition and PFC damage for ITER VDEs and MDs. The workflow methodology: 2D magnetic flux profiles from DINA simulations [3] provide input to the SMITER 3D field-line tracing software [4], producing 3D maps of perpendicular surface heat flux $q_\perp$ and magnetic field $\vec{B}$ on the FWPs. These maps are then used to compute time-dependent melt formation and motion with the MEMOS-U code [5,6], accounting for heat flux reduction by plasma vapor shielding [7]. This paper will analyze a selection of the VDE & MD dataset using the described analysis workflow.

2. DINA DISRUPTION DATASET

The DINA code computes magnetic equilibria and 1-D transport for the development of plasma scenarios and the analysis of plasma disruptions [3,8]. The appendix of [8] gives detailed descriptions of DINA's underlying equations, and a description of the power balance during VDEs and MDs is provided in [9]. These DINA disruption simulations start with an appropriate steady-state equilibrium scenario, and then perturb that equilibrium to initiate either a VDE or MD. In the case of an unmitigated (hot) VDE, a vertical perturbation is applied to the steady-state equilibrium and the plasma moves up or down. Once the last closed flux surface (LCFS) makes contact with the 2-D wall contour, the thermal quench (TQ) is triggered in DINA. At the time of the TQ, Be impurities are introduced instantaneously after the prescribed loss of the plasma thermal energy. The code then calculates the evolution of the current quench (CQ) phase, including halo current dynamics. Simulations of the MDs are similar, except that in this case the TQ is triggered before any plasma motion or FWP contact. Thus, the MDs have time to evolve and radiate away energy during the CQ phase before any contact with the wall.

The latest version of DINA, with updates described in [10], has been used to compile 84 ITER disruption scenarios relevant to PFPO-1 up to FPO. Variations in this disruption database include plasma current (I_p) and toroidal magnetic field (B_t), disruption direction (up or down), Be impurity density, cross-field thermal diffusivity coefficients (χ), and disruption type (VDE vs. MD). In these DINA simulations, no disruption avoidance or mitigation methods are assumed, such that maximum CQ time (t_{CQ}) and energy deposition are realized. The most important outputs from DINA are the time-dependent flux maps ($\Psi(r,z)$), the radial parallel heat flux distribution $q_\parallel(r)$ in the halo region, and the total energy E_{dep} deposited on the FW.

Variations in I_p and B_t match the q_{95} = 3 scenarios envisioned for PFPO: 5MA/1.8T, 7.5MA/2.65T, and 15MA/5.3T. The starting core plasma electron density n_e and temperature T_e are varied accordingly: $3 \cdot 10^{19}\ m^{-3}$ at 5MA, $5 \cdot 10^{19}\ m^{-3}$ at 7.5MA, and $10 \cdot 10^{19}\ m^{-3}$ at 15MA. For each of these scenarios (for both VDEs and MDs), there are at least two values for the assumed perpendicular transport coefficient χ: 1 m^2/s and 4 m^2/s. The Be impurity concentration, n_{Be}, is assumed uniform at the start of the TQ and varies from 0, $1 \cdot 10^{19}\ m^{-3}$, and $3 \cdot 10^{19}\ m^{-3}$. This impurity model in DINA is simple. In reality, n_{Be} in the plasma core and edge will vary in time and location as the VDE interacts with the first wall. This n_{Be} would be in addition to impurities present in the plasma during steady-state operations from sputtering/erosion of the FWPs. A self-consistent model of impurity introduction as the disruption evolves is not currently available in DINA. As discussed in Section 3 of [10], the maximum assumed n_{Be} is not unrealistic for a VDE originating from a 15MA, H-mode burning plasma scenario. For the lower power cases at 5MA, with a starting n_e of $3 \cdot 10^{19}\ m^{-3}$, an introduction of $n_{Be} = 3 \cdot 10^{19}\ m^{-3}$ would result in a mostly Be plasma (Z_{eff} = 3.4 post-TQ), but such plasmas may not be unreasonable based on observations on JET (Figure 8 of [11]) so they are covered here for consistency. Tungsten impurity (resulting from erosion of the divertor targets) is neglected due to its relatively low cooling power and the low expected core plasma concentrations (prior to the TQ).

2.1 Comparison of DINA halo current model with experiments

As covered in [10], the latest DINA version used to create this database incorporates a number of significant updates. The SMITER and MEMOS-U results in Sections 3 and 4 emphasize the influence of the disruption

dynamics on surface heat flux $q_\perp$, surface temperature rise, and melt damage. Therefore, it is important to keep in mind the assumptions made in the DINA model, as well as to compare with experimental observations where possible. Of particular importance is the accuracy of the halo current density J_h. Halo current dynamics play a strong role in calculating both electromagnetic and thermal loads [9,10]. The term halo width, w_h, is often used as a way to quantify the spatial distribution of J_h.

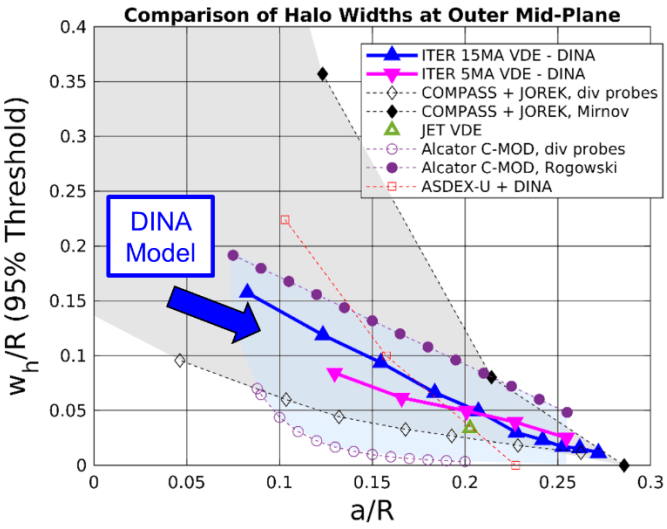

FIG. 1. Halo width w_h as a function of minor radius, normalized to device major radius. Experimental data is given with dashed lines, with solid markers for upper-bound data and open markers for lower bound data. DINA data for ITER is given by solid points and solid lines. As VDE or MD time increases, minor radius, a, decreases.

A unique first-attempt at comparing the DINA halo model to measurements of w_h across various tokamaks is given in [10]. In general, extrapolation of w_h data to ITER is not straightforward due to experimental differences in machine size and geometry, diagnostic limitations, and varying definitions of w_h used in publications. To compensate for these difficulties and limitations, w_h is defined as a physical width (in meters) mapped to the outer midplane (OMP) of the VDE plasma, with a cut-off point arbitrarily chosen as the last radial point at which the magnitude of J_h falls below 5% of the maximum. Mapping w_h along magnetic-field lines to the midplane eliminates differences in local wall geometry. Additionally, comparing w_h as a function of minor radius, a, compensates for large differences in VDE duration between devices. Finally, normalizing the values of w_h and minor radius (a) to the major radius (R), compensates for variations in machine size. Using this comparison methodology, the w_h data reported in [10] has been expanded and is given in Fig 1, which includes data from COMPASS [12,13], JET [14], Alcator C-MOD [15], and ASDEX-U [16,17]. Lower and upper bounds have been added for COMPASS (shaded in grey) as well as C-MOD (shaded in blue). In all cases, experimental data is coupled to simulation reconstructions of the VDE poloidal flux maps to estimate a and map J_h deposition locations back to the OMP.

The important conclusion is that w_h values from DINA fall within this wide range of experimental data. This builds confidence in the DINA predictions for w_h, $J_h(r)$ and $q_\parallel(r)$, which impact the magnitude and distribution of $q_\perp(r)$ in time. Still, it should be noted that there is a large uncertainty in the experimental data, particularly at the end of the VDE when a is small (and when $q_\perp$ is usually more severe). Continued effort by the fusion community to cross-compare halo current data across tokamak devices, using a common scaling and a fixed definition of w_h, is essential and strongly encouraged for extrapolation to ITER.

3. SMITER HEAT FLUX ANALYSIS

The next step in the workflow is a 3D heat flux analysis using the SMITER field-line tracing software [4]. SMITER utilizes the time dependent plasma equilibrium $\Psi(r,z)$, $q_\parallel(r)$, and E_{dep} from DINA. Magnetic field lines are traced from the 3D target geometries (in this case the Be FWPs and W divertor) to determine areas that are magnetically shadowed by upstream components. By relating the unshadowed field lines to $q_\parallel(r)$, and accounting for the field line intersection angle on the PFC surfaces, maps of $q_\perp$ are generated for any target PFC of interest. To guarantee that the 3D power balance in SMITER matches the 0-D power balance in DINA, a scaling factor is applied to $q_\parallel(r)$. This scaling takes into account the 3D, non-uniform power deposition observed in SMITER and also corrects the pitch angle definition of $q_\parallel$ within DINA to be $q_\parallel$ along the magnetic field lines. SMITER uses P_{halo}, the total power within the halo region (calculated based on E_{dep}), as the value for power in the scrape-off layer, P_{SOL}. The code does not dynamically account for power generation in the halo region and instead assumes that the entirety of P_{halo} is deposited onto the FW. The SMITER FWP geometries are smooth curved surfaces, as in [10] and [18], with a triangular mesh resolution of ~5mm.

A modest portion of the DINA disruption database has been evaluated in SMITER, 37 of 84 available cases. The selection covers the worst-case scenarios for ITER and is broad enough to study the importance of I_p/B_t, n_{Be}, χ, and disruption direction for both VDEs and MDs. During the CQ, the upward VDEs/MDs deposit all conducted

energy on the upper FWPs, meaning that FWPs #7, #8, and #9 at the top of the machine will assume the greatest risk of melt damage (see Fig 2). The downward VDEs/MDs deposit their energy on both the Be FWPs and on the outer baffle region of the W divertor vertical target. The power balance mentioned above does account for all components. However, the focus of this work is on the Be FWP material response. Work is ongoing at ITER for further evaluation of W melt damage using this analysis workflow.

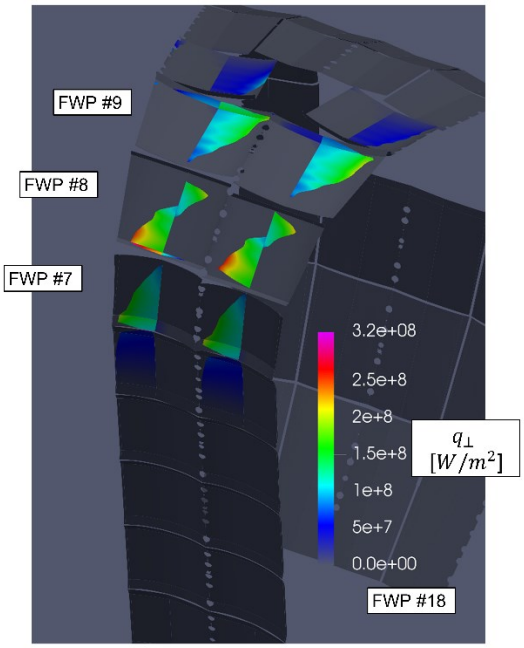

FIG. 2. Example map of $q_\perp$ calculated in SMITER for an entire poloidal sector of Be FWPs. The case is for a 15MA upward VDE ($n_{Be} = 3 \cdot 10^{19}\ m^{-3}, \chi = 1\ m^2/s$) at the time of max $q_\perp$ (Δt=200ms).

For upward disruptions, the peak heat flux, $q_{\perp,max}$, usually occurs towards the end of the CQ. This is when the plasma is smallest, causing the magnetic field lines to intersect at relatively large angles. E_{dep} also generally peaks near the end of the disruption which, when combined with larger field-line angles, further magnifies $q_{\perp,max}$. For downward cases, the LCFS usually limits on the divertor outer baffle. As the quenching plasma grows smaller and field-line intersection angles increase, the LCFS moves farther away from FWP #18. Since $q_\parallel(r)$ has an exponentially decreasing distribution (see [10]), this balances out to give a $q_{\perp,max}$ in the middle of the CQ, with $q_\perp$ decreasing as the plasma shrinks and quenches on the divertor. Thus, the downward VDEs are always less severe than their corresponding upward cases for the Be FWPs. In general, the VDE/MD time and heat flux intensity both increase with I_p and B_t. Consider the upward VDE as an example ($n_{Be} = 3 \cdot 10^{19}\ m^{-3}, \chi = 1\ m/s$). At 5MA/1.8T, the VDE lasts for ~75ms and deposits ~29MJ to the FW with $q_{\perp,max}$ ~83 MW/m^2. At 7.5MA/2.65T, those values increase to ~120ms, ~79MJ, and $q_{\perp,max}$ ~130 MW/m^2. Finally, for 15MA/5.3T, the VDE persists for ~250ms and deposits ~420MJ with $q_{\perp,max}$ ~320 MW/m^2. Figure 2 shows the 3D distribution of $q_\perp$ for this high current VDE at the time of $q_{\perp,max}$.

When comparing VDEs and MDs, the MDs often show a slightly higher energy deposition area, t_{CQ}, and E_{dep}. The value of χ has minimal impact on the VDE dynamics and heat flux when a non-zero n_{Be} is assumed. Scenarios with $\chi = 1\ m^2/s$ give slightly higher values of $q_\perp$, so only they are considered for the next step in the analysis. Conversely, the assumed n_{Be} has a strong effect on the disruption dynamics. Variation in n_{Be} significantly influences the t_{CQ}, E_{dep}, P_{halo}, and $q_{\perp,max}$ for all cases. Figure 3 highlights the impact of n_{Be} for upward VDE and MD scenarios. In general, a higher n_{Be} in the halo region leads to a shorter t_{CQ} and smaller magnitudes of total halo current I_{halo}. Radiative and ohmic losses are higher, causing less energy from the halo currents to be conducted along magnetic field-lines to the FW. However, a lower total E_{dep} over a shorter time can balance out to give increased $q_\perp$. For the previously described 15MA/5.3T VDE ($n_{Be} = 3 \cdot 10^{19}\ m^{-3}, \chi = 1\ m^2/s$), lowering n_{Be} to $1 \cdot 10^{19}\ m^{-3}$ increases t_{CQ} to ~400 ms and E_{dep} to ~590 MJ. The $q_{\perp,max}$ over that longer timespan reduces slightly, to ~307 MW/m^2. The same relationships with n_{Be} are observed for the MD scenarios to a more pronounced degree. For the MDs ('cold' VDEs), the TQ and its associated influx of Be impurities occurs before the plasma makes contact with the FW.

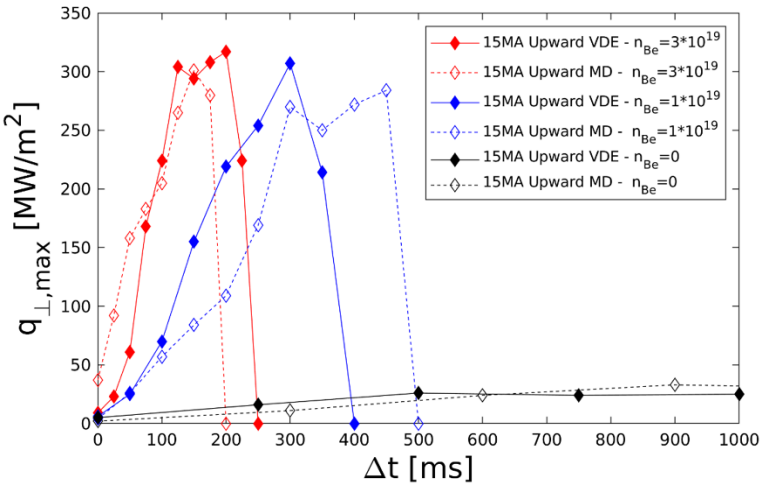

FIG. 3. Maximum surface heat flux $q_{\perp,max}$ vs disruption time. VDE data is given by solid lines, with the corresponding MDs given by dashed lines of the same color. Data for the cases of $n_{Be} = 0$ extend outside of the plot, up to ~2750ms and 3300ms for the VDE and MD, respectively. Δt=0 represents the point at which E_{dep} becomes > 1MJ.

The DINA disruption scenarios assuming n_{Be} = 0 give an extremely long t_{CQ}. The same 15MA, $\chi = 1$ VDE case with $n_{Be} = 0$ lasts for almost 3 seconds. With no radiative energy loss, a full ~940 MJ of conductive energy is calculated for the FW. This energy deposition over such a long time-span produces peak heat fluxes of $\sim 55\ MW/m^2$. The radiation loss term is a vital component to the DINA power balance (see Eq. 2 of [9]), and any disruption will introduce Be (and W) impurities during both the TQ and CQ phases. For these reasons, the scenarios for $n_{Be} = 0$ need not be considered for the next step in the analysis.

4. MEMOS-U MELT DAMAGE

The MEMOS-U melt dynamics code predicts the formation and motion of molten Be on the ITER FWPs [5,6]. The code solves the incompressible resistive thermoelectric MHD equations in the magnetostatic limit, along with the convection-diffusion equation for temperature. References [5,6] detail the physics of boundary conditions, which depend on the plasma scenario and the material composition. Material properties for solid and liquid Be are compiled for MEMOS-U with sources listed in [5,18]. For energy deposition during the CQ phase of a disruption, melt motion is driven by a volumetric $\vec{J_h} x \vec{B}$ force within the shallow (~mm) melt layer. MEMOS-U requires the 3D maps of $q_\perp$ and $\vec{B}$ vectors from SMITER as input. I_{halo} is calculated from DINA at each timestep, and then evenly distributed as a density $\vec{J_h}(x, y)$ across the total wetted area calculated in SMITER. In reality, $\vec{J_h}$ will vary across this wetted area and will depend on the parallel current density $\vec{J}(r)$ within the halo region. The directionality of $\vec{J_h}$ is properly implemented as the halo current flows into the FWPs on one side of the LCFS contact point and flows out of the FWPs on the other side. This characteristic of $\vec{J_h}$ leads to different flow directions on either side of the LCFS contact point (see Fig 6). For all results presented here, the MEMOS-U rectangular domain resolution is 0.5 x 0.5 cm across the FWP surface, to match the SMITER mesh lengths.

It should be emphasized that macroscopic melt motion of Be has been clearly documented on JET [19] and poses a legitimate risk to the ITER FWPs. During the first JET ITER-Like Wall campaigns, a handful of upward going unmitigated VDEs led to macroscopic motion of Be on the limiter tiles at the top of the main chamber, or 'dump plates.' The melt layers were observed to move poloidally from the inboard side to the outboard side. The same directions of I_p and B_t in these JET discharges will be used for ITER. The $\vec{J_h}$ flow directions in this paper match the JET observations, with Be melt on the outboard side of the LCFS flowing in the outboard direction. MEMOS-U has recently been used to successfully model the observed melt damage on the JET dump plates [6], which builds confidence in the results presented for ITER in Section 4.2.

4.1 Vapor shielding in MEMOS-U

One unique aspect of this work is the incorporation of a vapor shielding model in MEMOS-U. As heat and particle fluxes impact the FWP material surface, individual Be atoms are ejected from the surface via sputtering, evaporation, and/or ablation. Such ejection forms a vapor layer of Be just above that surface. This layer is then ionized and excited via successive heat and particle fluxes, ultimately 'shielding' the underlying surface by reducing the impinging fluxes. The presence of a vapor shield can reduce the surface temperature rise, which can in turn lessen the thickness of any melt layer formation and thereby reduce the $\vec{J} x \vec{B}$ displacement volume.

The PIXY code uses a Particle-in-Cell (PIC) model for the plasma, accounting for edge plasma properties and sheath physics up to a solid surface [7]. The motion and interactions of electrons, hydrogen ions, and wall-derived vapor particles are solved in 1D space but with 3D velocity (1d3v). A 1-D heat transfer model is coupled to PIXY to estimate the surface temperature, T_{surf}, in this case a Be FWP model with 10mm of Be, 7mm of copper, and cooling water at 343 K. Dedicated PIXY simulations have been performed for the ITER disruption energy deposition analysis workflow [20]. VDE parameters from DINA VDE scenarios at 5MA, 7.5MA, and 15MA are used as input for a range of PIXY simulations, such as n_e, T_e, $\vec{B}$ magnitude and average impact angle (see Table 1 of [20]). Due to the heavy computational requirements of PIC simulations and long VDE times (hundreds of ms), a simple implementation is chosen. An analytic function for the vapor shielding efficiency ε_{VS} as a function T_{surf} and $q_\perp$ is calculated for each value of I_P. These functions are implemented in MEMOS-U for interpolation. The PIXY datasets cover T_{surf} = 1400 – 2200 K (the melting point of Be is ~1560 K) and $q_\perp = 50 - 1000\ MW/m^2$.

At each time point in the MEMOS-U simulations, a reduction in the SMITER $q_\perp$ value is performed at each mesh point based on ε_{VS}, when vapor shielding is turned 'on'. This implementation scheme is valid so long as the MEMOS-U time steps are much longer than the equilibration time of the vapor shield. PIXY simulations establish the vapor shield on the order of tens of us, and the MEMOS-U results in Section 4.2 use a temporal resolution on the order of ~ms. The other inherent assumption is that the vapor shield calculated above each ~5mm mesh grid stays in place over the MEMOS-U time step. Temporal and spatial motion of the Be vapor cloud cannot be calculated in PIXY, and would require a different modeling scheme such as the TOKES code [21]. For the worst-

case VDE/MD scenarios from Section 3, ε_{vs} values up to 0.5 are observed by the end of the disruption. $\varepsilon_{VS} = 1$ implies a full reduction of $q_{\perp}$ to 0.

4.2 MEMOS-U results

Any variation in the time or total energy deposition will strongly influence melt occurrence and dynamics. The severity of melt damage heavily depends on when during the disruption process the Be surface reaches its melt temperature. Any additional, sufficiently high heat flux can cause the melt layer to increase in depth. Then, volumetric $\vec{J_h} x \vec{B}$ forces within that melt layer will cause macroscopic lateral motion of the melt. Removal of the upper layers of molten Be in areas of continued energy deposition will lead to enhanced heat conduction and melt generation [6]. The resulting melt damage takes the form of excavated pits, where a thickness of Be has been displaced outside the melt pool and resolidified. Thus, the timing of when T_{surf} exceeds the melt threshold matters greatly with respect to the VDE/MD duration. More severe melt damage will occur for cases that reach the melt threshold early-on in the disruption.

MEMOS-U simulations were completed for 16 of the SMITER results, with an emphasis on cases with $n_{Be} = 1 \cdot 10^{19}\ m^{-3}$. Simulation time was extended past the disruption duration long enough for the 3D melt deformations to stop moving and resolidify, ~100-200ms. Figure 4 summarizes the MEMOS-U analysis efforts, which were conducted for multiple FWPs (#7-9 and #18), with and without the vapor shielding model discussed in Section 4.1.

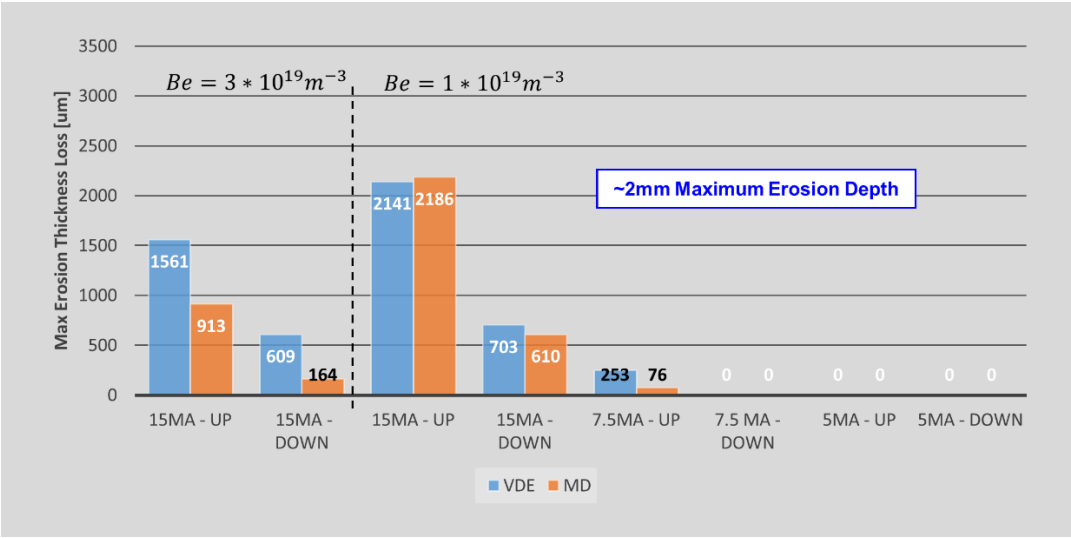

FIG. 4. MEMOS-U results for maximum erosion thickness loss. The VDE for each scenario is shown by the left, blue bar, and the corresponding MD is shown by the right, orange bar. Cases with $n_{Be} = 3 \cdot 10^{19}\ m^{-3}$ and $1 \cdot 10^{19}\ m^{-3}$ are shown to the left and right, respectively, of the vertical dashed line.

The damage metric used here is the maximum depth of material loss across the entire FWP surface. For all upward cases, the greatest erosion depth is found on FWP #8. For all downward events, melt damage occurs only on FWP #18. The first key observation from Fig. 4 is that no melt damage is found for all 5MA cases (independently of n_{Be}). This was also true for the cases reported in [10]. At 7.5MA, only the upward VDE with $n_{Be} = 1 \cdot 10^{19}\ m^{-3}$ shows significant melt damage. This is encouraging in showing that the very extensive DMS commissioning planned in the ITER Research Plan in PFPO-1 can be conducted up to I_p at the 5 MA level without fear of significant damage to the FW. It also demonstrates that for the extensive H-mode operation at 7.5 MA planned in PFPO-2, the DMS will need to achieve a high degree of reliability for CQ mitigation.

Substantial melt damage is observed for all 15MA VDE and MD cases. At higher n_{Be} ($3 \cdot 10^{19} m^{-3}$), the VDE scenarios are more damaging than the MDs. The higher impurity densities allow for more plasma energy to radiate away at the start of the CQ, before the MD can contact the FW and begin depositing conductive energy. At lower n_{Be} ($1 \cdot 10^{19}\ m^{-3}$), the MD-induced melt damage is similar to the VDE cases. As stated in Section 3, the MD deposits more energy to the first wall than VDE, but over a longer t_{CQ} and with slightly lower $q_{\perp,max}$. In MEMOS-U, this balances out to give the MD a similar erosion depth to the corresponding VDE. For the upward 15MA case, the melt volume displacement is ~25% higher for the MD than for the VDE due to the increased FWP wetted area. Based solely on the erosion thickness losses, the worst-case scenarios for ITER are the upward 15MA disruptions with $n_{Be} = 1 \cdot 10^{19}\ m^{-3}$ and $\chi = 1\ m^2/s$. With vapor shielding included, both the VDE and MDs result in a maximum erosion thickness loss of ~2 mm. This is ~30% lower than would be the case if shielding was

not accounted for (~3mm). For all VDEs & MDs in Figure 4 with melt damage, the inclusion of vapor shielding reduced the erosion thickness loss by 20-40%.

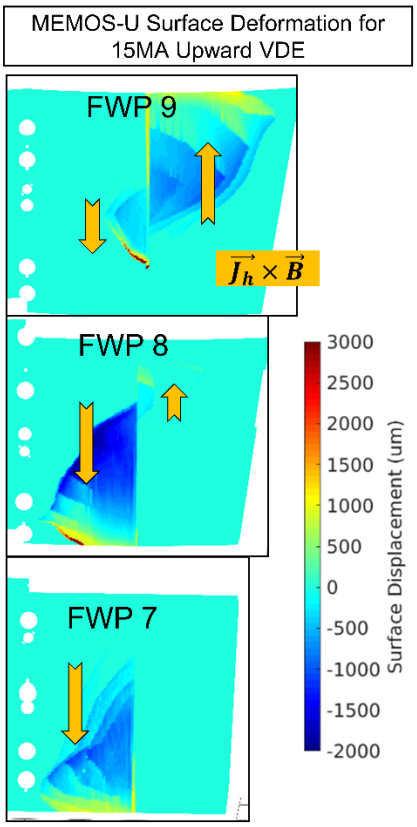

FIG. 5. 3D maps of surface deformation on upper FWPs for the worst-case 15MA upward VDE. Yellow arrows indicate the $\vec{J_h}x\vec{B}$ direction for a given melt area.

deposition of $q_{\perp}$ and $\vec{J_h}$ at such high T_{surf} is what facilitates melt erosion thickness losses on the order of ~mm. Interpolating in Fig. 6 indicates that values of I_p up to ~7 MA may be tolerable with respect to FWP CQ-induced melt damage.

5. CONCLUSIONS

Energy deposition and melt damage analysis has been performed for current quenches of a wide range of ITER VDEs and MDs. The t_{CQ}, E_{dep}, and $q_{\perp,max}$ of the disruptions increase substantially with increasing I_p. The 15MA/5.3T disruptions show the most extreme melt damage out of the three q_{95} = 3 pairs of I_p/B_t considered. For a given I_p, DINA modeling and SMITER field-line tracing indicate that the assumed n_{Be} injected at the start of the CQ plays a major role in the disruption dynamics. Time-dependent MEMOS-U simulations, including vapor shielding, are necessary to determine whether or not each disruption can induce macroscopic melt damage. The new DINA-SMITER-MEMOS-U workflow has provided an invaluable tool for assessment of when in the ITER Research Plan disruption mitigation becomes mandatory from the point of view of PFC melt damage. An important conclusion is the identification of a clear operating window with $I_p \lesssim 7$ MA in which PFC melting may be avoided even without disruption current quench mitigation.

Figure 5 shows the 3D distribution of the surface displacement across FWPs #7-9 after the worst-case 15MA VDE. Negative values (in blue) represent erosion thickness loss where material is excavated from the original surface and positive values (in yellow and red) represent build-up of molten Be as it is poloidally displaced. The yellow arrows denote the general direction of melt flow. As discussed previously, the $\vec{J_h}x\vec{B}$ force direction changes depending on whether the halo current is flowing into or out of the FWP wetted area. An important observation in Fig 5 is the areal extent of melt damage. Waves of molten Be travel on the order of tens of cm in these simulations, in some cases running off the FWP edges and outside the computational domain. This is analogous to the 'Be waterfall' observed in [19] and modeled in [5]. More importantly for ITER, the Be FWPs are not smooth as in the SMITER models but are castellated. Such extensive Be motion will lead to gap-bridging within the castellated fingers of the damaged panels, which was also observed on JET.

Figure 6 compiles the time dependence of the maximum T_{surf} found on the FWPs for the upward going CQ scenarios in Fig 4. The upward 5MA VDE and MD cases stay well below the melt threshold, reaching ~1230 K and 1050 K, respectively. At 7.5MA, the VDE and MD cases each last for ~200ms, with the melt threshold exceeded only at the end of the CQ. This minimizes the melt and motion that can occur before the surface cools and resolidifies. The 15MA upward cases sustain a maximum temperature of ~2300 K over hundreds of ms. The sustained

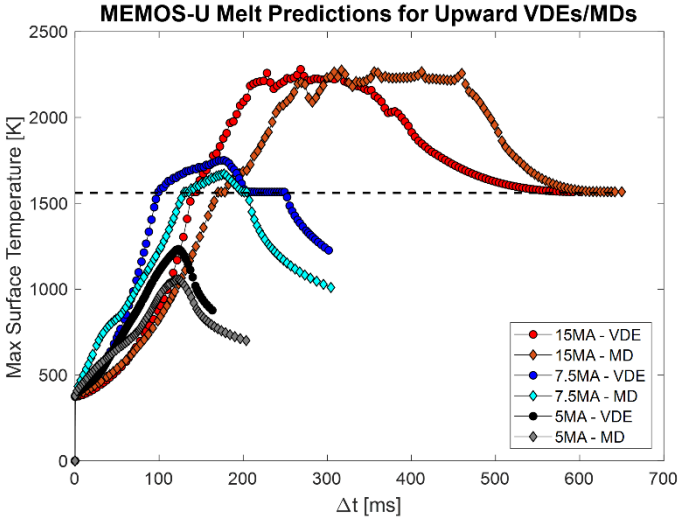

FIG. 6. Maximum surface temperature vs time for upward VDEs (with circular markers) and MDs (with diamond markers). $n_{Be} = 1 \cdot 10^{19}\ m^{-3}$ and $\chi = 1\ m^2/s$ for all cases (vapor shielding included). The black dashed line marks the melt temperature for Be at 1560K. MEMOS-U simulation times are longer than the VDE/MD time to allow for re-solidification of melt damage.

This corresponds to the majority of the L-mode operation range currently foreseen in the first ITER non-active operation phase. The analysis also clearly demonstrates that first wall melt damage can be very severe at high I_p. By the time planned attempts are made to achieve 15 MA L-mode plasmas in PFPO-2 and burning plasmas in FPO, the DMS much reach extremely high levels of robustness and reliability.

ACKNOWLEDGEMENTS

ITER is the Nuclear Facility INB No. 174. This publication explores physics processes during the plasma operation of the tokamak when disruptions take place; nevertheless, the nuclear operator is not constrained by the results presented here. The views and opinions expressed herein do not necessarily reflect those of the ITER Organization. The work of EM was supported by MEYS project 8D15001 and LM2018117. SR would like to acknowledge the financial support of the Swedish Research Council under Grant No. 2018-05273.

REFERENCES

[1] ITER Research Plan Within the Staged Approach (Level III), https://www.iter.org/technical-reports
[2] R.A. Pitts et al., Physics basis for the first ITER tungsten divertor, Nuclear Materials & Energy, 20 (2019) 100696
[3] V. E. Lukash and R. R. Khayrutdinov, Plasma Physics Reports 22 (1996) 91
[4] L. Kos et al., Fus. Eng. Des, 146 B (2019) 1796
[5] E. Thoren et al, Plasma Phys. Control. Fus. 63 (2021) 035021
[6] S. Ratynskaia et al, Nuclear Fusion 60 (2020) 104001
[7] K. Ibano et al, Nuclear Fusion 59 (2019) 076001
[8] S. Miyamoto et al., Nuclear Fusion 54 (2014) 083002
[9] D.I. Kiramov et al, 43rd EPS conference on plasma physics, P4.071 http://ocs.ciemat.es/EPS2016PAP/pdf/P4.071.pdf
[10] J. Coburn et al, Reassessing energy deposition for the ITER 5 MA vertical displacement event with an improved DINA model, Nuclear Mat. & Energy, accepted for publication (2021)
[11] G. Matthews et al, Journal of Nuclear Materials 438 (2013) S2–S10
[12] F. J. Artola et al., Plasma Physics and Controlled Fusion (2021), in press https://doi.org/10.1088/1361-6587/abf620
[13] M. Hoelzl et al., submitted to Nuclear Fusion (2021) https://arxiv.org/abs/2011.09120
[14] V. Riccardo et al., Nuclear Fusion 49 (2009) 055012
[15] R. A. Tinguely et al., Nuclear Fusion 58 (2018) 016005
[16] G. Pautasso et al, Nuclear Fusion 51 (2011) 043010
[17] G. Pautasso et al, Nuclear Fusion 51 (2011) 103009
[18] J. Coburn et al., Phys. Scr. T171 (2020) 014076
[19] I. Jepu et al., Nuclear Fusion 59 (2019) 086009
[20] K. Ibano et al, Vapor shielding efficiency of beryllium first wall during ITER vertical displacement events, in preparation for Physics of Plasmas (2021)
[21] S. Pestchanyi and F. Maviglia, Nuclear Fusion 24 (2020) 100767